Available online at www.sciencedirect.com
SCIENCE DIRECT
Physics of the Earth and Planetary Interiors 156 (2006) 59–74
PHYSICS OF THE EARTH AND PLANETARY INTERIORS
www.elsevier.com/locate/pepi

Seismic implications of mantle wedge plumes

Taras V. Gerya [a,b,*], James A.D. Connolly [a], David A. Yuen [c], Weronika Gorczyk [a], Allison M. Capel [c]

[a] *Department of Earth Sciences, Swiss Federal Institute of Technology (ETH - Zürich), CH-8092 Zurich, Switzerland*
[b] *Institute of Experimental Mineralogy, Russian Academy of Sciences, 142432 Chernogolovka, Moscow, Russia*
[c] *University of Minnesota Supercomputing Institute, Department of Geology and Geophysics, University of Minnesota, Minneapolis, MN 55455-0219, USA*

Received 20 September 2005; received in revised form 24 January 2006; accepted 1 February 2006

Abstract

We use a coupled petrological–thermomechanical model to investigate the dynamical effects of metamorphic reactions and melting on the seismic structure of thermal–chemical plumes beneath volcanic arcs. Plume generation is driven by the subduction of buoyant crustal rocks and expulsion of aqueous slab fluids that causes hydration and partial melting of the mantle wedge. The model demonstrates two chemically distinct types of plumes. Unmixed plumes initiate from the melting front within the mantle that arises as a consequence of infiltration of slab-derived water-rich fluids, whereas mixed plumes initiate from the slab itself and entrain both slab- and mantle-derived magmas. Mixed plumes explain magmas such as adakites with crustal signatures, while primitive arc tholeiites are attributed to unmixed plumes. As a consequence of the interplay between water content and temperature both positive and negative seismic velocity anomalies are associated with the plumes. Positive anomalies are prevalent close to the slab due to the lowered temperatures associated with regions of cold plume initiation. Negative seismic anomalies develop at shallower depth due to the partially molten rocks that form plume heads. Flat lying partially molten regions that form beneath volcanic arcs as a consequence of cold wet plumes are manifest by >20% variations in the local Poisson ratio, as compared to variations of ∼2% expected as a consequence of temperature variation within the mantle wedge. In contrast to models that attribute a purely thermal origin for mantle wedge seismic anomalies, the petrological–thermomechanical model is able to explain the strong seismic velocity variations existing beneath volcanic arcs.

Keywords: Subduction zones; Numerical modeling; Seismic tomography; Partial melting; Mantle plumes; Volcanic arcs

1. Introduction

Seismic structures with strong both positive and negative velocity anomalies in the mantle wedge above subduction zones (Zhao et al., 2002; Tamura et al., 2002) have been interpreted as thermally (Tamura et al., 2002) or chemically (e.g., Jung and Karato, 2001) induced phenomena. In this study, we employ numerical models to examine an alternative hypothesis that these anomalies are caused by the plume-like structures that (Gerya and Yuen, 2003a; Gerya et al., 2004a) evolve from the subducted plate. For this purpose we develop a coupled petrological–thermomechanical model that allows us to predict seismic velocity anomalies in the wedge. Previous models of the seismic structure of

* Corresponding author. Tel.: +41 44 6337539; fax: +41 44 6321080.
E-mail addresses: taras.gerya@erdw.ethz.ch (T.V. Gerya), daveyuen@gmail.com (D.A. Yuen).

0031-9201/$ – see front matter © 2006 Elsevier B.V. All rights reserved.
doi:10.1016/j.pepi.2006.02.005

subduction zones (e.g., Peacock and Wang, 1999; Zhao, 2001; Connolly and Kerrick, 2002; Hacker and Abers, 2004) were based on prescribed thermal and lithological structures and/or assumed mineralogical distributions. In contrast, we employ a thermodynamic model to compute mineralogies and their physical properties, including compressional and shear wave velocities, from the thermal and chemical fields obtained by geodynamical modeling. The computed rock properties, such as density, heat capacity, thermal expansion and water content, feedback in turn on the geodynamic evolution.

In previous work (Gerya and Yuen, 2003a) we demonstrated that hydration and partial melting along the subducting slab can trigger Rayleigh–Taylor instabilities that evolve into partially molten diapiric structures ("cold plumes"). However, our previous model did not account for the effects of metamorphic reactions on the dynamics of slab dehydration and mantle melting. Incorporation of the thermodynamic model in the present work allows us to explore this effect and in particular to test whether the model is able to explain the seismic velocity variations observed in mantle wedges beneath volcanic arcs.

2. Petrological model

The model oceanic crust consists of a relatively thin (1000 m) heterogeneous layer of marine sediments, an upper 2 km thick sequence of hydrothermally altered basalts (metabasalts), and a lower 5 km section comprised largely of gabbroic rocks (Table 1). The subjacent mantle is considered to be anhydrous peridotite, whereas the overlying mantle is either anhydrous or

Table 1
Model rock compositions (weight %)

	Sediment	Upper oceanic crust (altered basalt)	Lower oceanic crust (gabbro)	Mantle (peridotite)
SiO_2	61.10	47.62	53.49	45.55
Al_2O_3	12.43	14.48	14.07	4.03
FeO	5.43	10.41	6.86	7.47
MgO	2.59	6.92	12.07	37.42
CaO	6.21	13.39	10.73	3.18
Na_2O	2.54	2.15	1.22	0.33
K_2O	2.13	0.58	0.09	0.03
H_2O[a]	7.60	2.78	1.47	1.98

Sediment is the GLOSS average (Plank and Langmuir, 1998); basalt is an average for the upper 500 m of the igneous section of the oceanic crust (Staudigel et al., 1989); gabbro is a synthetic composition for the gabbroic section of the oceanic crust (Behn and Kelemen, 2003), modified to contain up to 1.5 wt.% water to represent the effects of lower crustal hydrothermal alteration (Carlson, 2003), and peridotite is the LOSIMAG composition (Hart and Zindler, 1986) chosen to represent mantle peridotite. The compositions have been simplified by the omission of minor elements such as Mn, P, Ti, and Cr and the assumption that all Fe is ferrous, additionally CO_2 has been removed from the GLOSS sediment composition.

[a] Maximal H_2O content in the rocks (cf. Section 2 for details of water balance at elevated P and T).

Table 2
Phases and thermodynamic data sources

Phase	Formula	Source
Antigorite	$Mg_{48x}Fe_{48(1-x)}Si_{34}O_{85}(OH)_{62}$	Rupke et al. (2004)
Clinoamphibole	$Ca_{2-2w}Na_{z+2w}Mg_{(3+2y+z)x}Fe_{(3+2y+z)(1-x)}Al_{3-3y-w}Si_{7+w+y}O_{22}(OH)_2$, $w+y+z \le 1$	Wei and Powell (2003); White et al. (2003)
Biotite	$KMg_{(3-w)x}Fe_{(3-w)(1-x)}Al_{1+2w}Si_{3-w}O_{10}(OH)_2$, $x+y \le 1$	Powell and Holland (1999)
Chlorite	$Mg_{(5-y+z)x}Fe_{(5-y+z)(1-x)}Al_{2(1+y-z)}Si_{3-y+z}O_{10}(OH)_8$	Holland et al. (1998)
Coesite	SiO_2	
Clinopyroxene	$Na_{1-y}Ca_yMg_{xy}Fe_{(1-x)y}Al_ySi_2O_6$	Holland and Powell (1996)
Fluid	H_2O	Holland and Powell (1998)
Garnet	$Fe_{3x}Ca_{3y}Mg_{3(1-x-y)}Al_2Si_3O_{12}$, $x+y \le 1$	Holland and Powell (1998)
Kyanite	Al_2SiO_5	
Lawsonite	$CaAl_2Si_2O_7(OH)_2 \cdot (H_2O)$	
Mica	$K_xNa_{1-x}Mg_yFe_zAl_{3-2(y+z)}Si_{3+y+z}O_{10}(OH)_2$	Holland and Powell (1998)
Melt	Na–Mg–Al–Si–K–Ca–Fe hydrous silicate melt	Ghiorso et al. (2002)
Olivine	$Mg_{2x}Fe_{2(1-x)}SiO_4$	Holland and Powell (1998)
Orthopyroxene	$Mg_{x(2-y)}Fe_{(1-x)(2-y)}Al_{2y}Si_{2-y}O_6$	Holland and Powell (1996)
Plagioclase	$Na_xCa_{1-x}Al_{2-x}Si_{2+x}O_8$	Newton et al. (1980)
Sanidine	$Na_xK_{1-x}AlSi_3O_8$	Thompson and Hovis (1979)
Stishovite	SiO_2	
Talc	$Mg_{(3-y)x}Fe_{(3-y)(1-x)}Al_{2y}Si_{4-y}O_{10}(OH)_2$	Holland and Powell (1998)

Unless indicated otherwise thermodynamic data was taken from (Holland and Powell, 1998) (revised 2002). The compositional variables w, x, y, and z may vary between zero and unity and are determined as a function of pressure and temperature by free energy minimization. Thermodynamic data for the iron endmember for antigorite solution was estimated as described in reference (Rupke et al., 2004).

hydrated (≤2 wt.% water) peridotite depending on the kinematic model for the propagation of slab fluids discussed below. Although mantle wedge rocks have the capacity to absorb up to 8 wt.% water during serpentinization (Connolly, 2005), we adopt 2 wt.% water as an upper limit to account for incomplete and heterogeneous hydration (Peacock, 1987) resulting from channelization of slab-derived fluids (Davies, 1999). Water contents in this ranger are also consistent with observed mantle wedge seismic velocities (Bostock et al., 2002; Carlson and Miller, 2003).

The stable mineralogy for each lithology were obtained by free energy minimization (Connolly, 2005) as a function of pressure and temperature from thermodynamic data (Table 2). For this purpose, phase relations were resolved on a grid with a resolution of 5 K and 25 MPa. The range of physicochemical conditions considered here requires extrapolation of the silicate melt model (Ghiorso et al., 2002). Therefore, to ensure consistency with experimentally constrained melting boundaries employed in our earlier work (Gerya and Yuen, 2003a), calculations were done for each lithology both with and without the silicate melt model. Physical properties were then computed from the appropriate results depending upon whether melt was predicted to be stable from the experimentally constrained phase relations (Table 3).

Seismic velocities were calculated as outlined by (Connolly and Kerrick, 2002), with shear moduli as summarized in (Connolly, 2005). In the absence of textural information, aggregate elastic moduli are typically computed as an equally weighted combination of the geometric and arithmetic means of the moduli of the constituent minerals, i.e., Voigt–Reuss–Hill averaging (Bina and Helffrich, 1992). Because the geometric mean vanishes if a constituent modulus approaches zero, as is the case for the shear modulus of the melt, the Voigt–Reuss–Hill scheme leads to profound shear wave velocity anomalies even if the amount of melt is negligible. As we are concerned with the prediction of such anomalies, we have computed aggregate velocities from volumetrically weighted arithmetic mean moduli. This approach assures a conservative model in that it minimizes the effect we are attempting to simulate. The aggregate velocities include the effects of silicate melt but do not account for the presence of free water, the amount of which is assumed to be negligible. The seismic velocities for sediment and hydrous peridotite (Fig. 1) demonstrate that although subsolidus phase transitions have a significant effect on velocity, this effect pales in comparison to that resulting from melting. The terraced variation in velocities within the melt field for hydrated peridotite (Fig. 1a and b) is primarily an artifact resulting from the coarse resolution of melt composition specified for the calculation. In contrast, the larger steps evident in the velocity field for the sedimentary lithology (Fig. 1c and d) primarily reflect supra-solidus phase transitions.

At the onset of subduction the lithologies in the oceanic crust are assigned the water contents indicated in Table 1 and the surrounding mantle is anhydrous. To simulate the migration of water released by dehydration reactions, if water is found to be a stable phase at a particular depth the water is propagated instantaneously upward, until it reaches a rock which contains amount

Table 3
Material properties used in 2D numerical experiments

Material	Thermal conductivity (W/(m K))	Rheology	P–T conditions of wet solidus
Sedimentary rocks	$0.64+\frac{807}{T+77}$	Wet quartzite flow law	$889+\frac{17900}{P+54}+\frac{20200}{(P+54)^2}$ at $P<1200$ MPa, $831+0.06P$ at $P>1200$ MPa
Upper oceanic crust (altered basalt)	$1.18+\frac{474}{T+77}$	Wet quartzite flow law	$973-\frac{70400}{P+354}+\frac{77800000}{(P+354)^2}$ at $P<1600$ MPa, $935+0.0035P+0.0000062P^2$ at $P>1600$ MPa
Lower oceanic crust (gabbro)	-//-	Plagioclase (AN_{75}) flow law	-//-
Serpentinized mantle	$0.73+\frac{1293}{T+77}$	Constant viscosity, 10^{18}–10^{19} Pa s	–
Hydrated unserpentinized mantle[a]	-//-	Wet olivine flow law	$1240+\frac{49800}{P+323}$ at $P<2400$ MPa, $1266-0.0118P+0.0000035P^2$ at $P>2400$ MPa
Dry mantle	-//-	Dry olivine flow law	–
References	Clauser and Huenges (1995)	Gerya et al. (2002), Ranalli (1995)	Schmidt and Poli (1998), Poli and Schmidt (2002)

[a] Hydrated mantle beyond the serpentine stability field (Schmidt and Poli, 1998), $T>751+0.18P-0.000031P^2$ at $P<2100$ MPa, $T>1013-0.0018P-0.0000039P^2$ at $P>2100$ MPa.

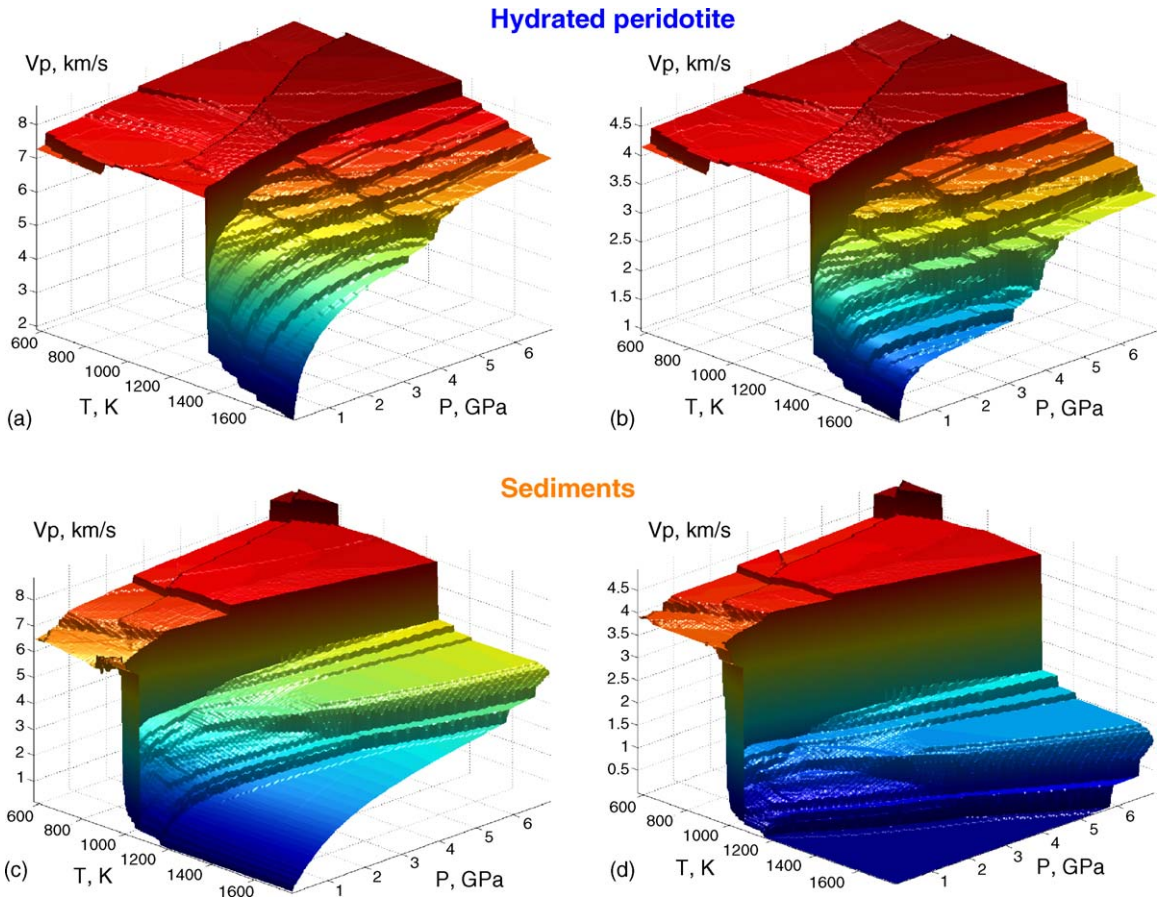

Fig. 1. Computed shear (v_s) and compressional (v_p) wave velocities for (a and b) hydrated peridotite and (c and d) sediments as a function of pressure and temperature. The abrupt decrease in seismic velocities at temperatures of 1000–1200 K is due to the presence of silicate melt.

of water which is less than: (i) upper limit of water content adopted for this specific rock type (Table 1) or (ii) the amount of water that can be consumed by all water-bearing minerals of the equilibrium mineral assemblage stable in the rock. Although the limits of water content are to some degree arbitrary, this approach provides a rough estimate for the position of the hydration front that develops in the mantle wedge as a result of slab devolatilization. To formulate this process analytically we compute the vertical velocity of the hydration front from the transport equation (Gerya et al., 2002)

$$\frac{\partial z_{h(x)}}{\partial t} = v_z - \frac{v_x \partial z_{h(x)}}{\partial x} - v_{h(x)}, \tag{1}$$

where $z_{h(x)}$ is the depth of the hydration front at the horizontal coordinate x, $v_{h(x)}$ the substantive hydration rate along the hydration front and v_z and v_x are the vertical and horizontal components of the material velocity vector at the hydration front. To obtain $v_{h(x)}$, the mass balance equation for water as

$$\int_{z=z_{h(x)}}^{z_{max}} \frac{D(X_{H_2O(x,z)})}{Dt} \rho_{(x,z)}\, dz = -v_{h(x)} X_{H_2O(x,z_{h(x)})} \rho_{(x,z_{h(x)})}, \tag{2}$$

where z is depth (z_{max} corresponds to the lower boundary of the model); $X_{H_2O(x,z)}$ and $\rho_{(x,z)}$ are the local water content (weight fraction) and density (kg/m^3) of the rocks beneath the hydration front; $X_{H_2O(x,z_{h(x)})}$ and $\rho_{(x,z_{h(x)})}$ are, respectively, water contents and density of hydrated mantle on the hydration front; D/Dt represents the substantive time derivative computed for moving rocks by using a marker method. Eqs. (1) and (2) are solved after each time step of the thermomechanical model, using the densities and water contents determined by free energy minimization for the relevant lithologies and pressure–temperature conditions. In addition to water-bearing minerals at low temperature ($T < 573$ K) and pressure ($P < 1$ GPa), free water is present in sedi-

ments and basaltic crust. Pore water content ($X_{H_2O(p)}$) is assumed to decrease linearly with both P and T as

$$X_{H_2O(p)} = X_{H_2O(p0)} \left(\frac{573 - T_{(K)}}{300} \right) \times \left(1 - P_{(GPa)} \right), \quad (3)$$

where $X_{H_2O(p0)}$ is the water content at $T = 273$ K and $P = 0.1$ MPa. Here we conservatively estimate $X_{H_2O(p0)} = 2$ wt.% for both sediments and basaltic crust. Eq. (3) limits the influence of connate fluid to low temperatures. At the higher temperatures relevant for plume generation the water present in connate fluids

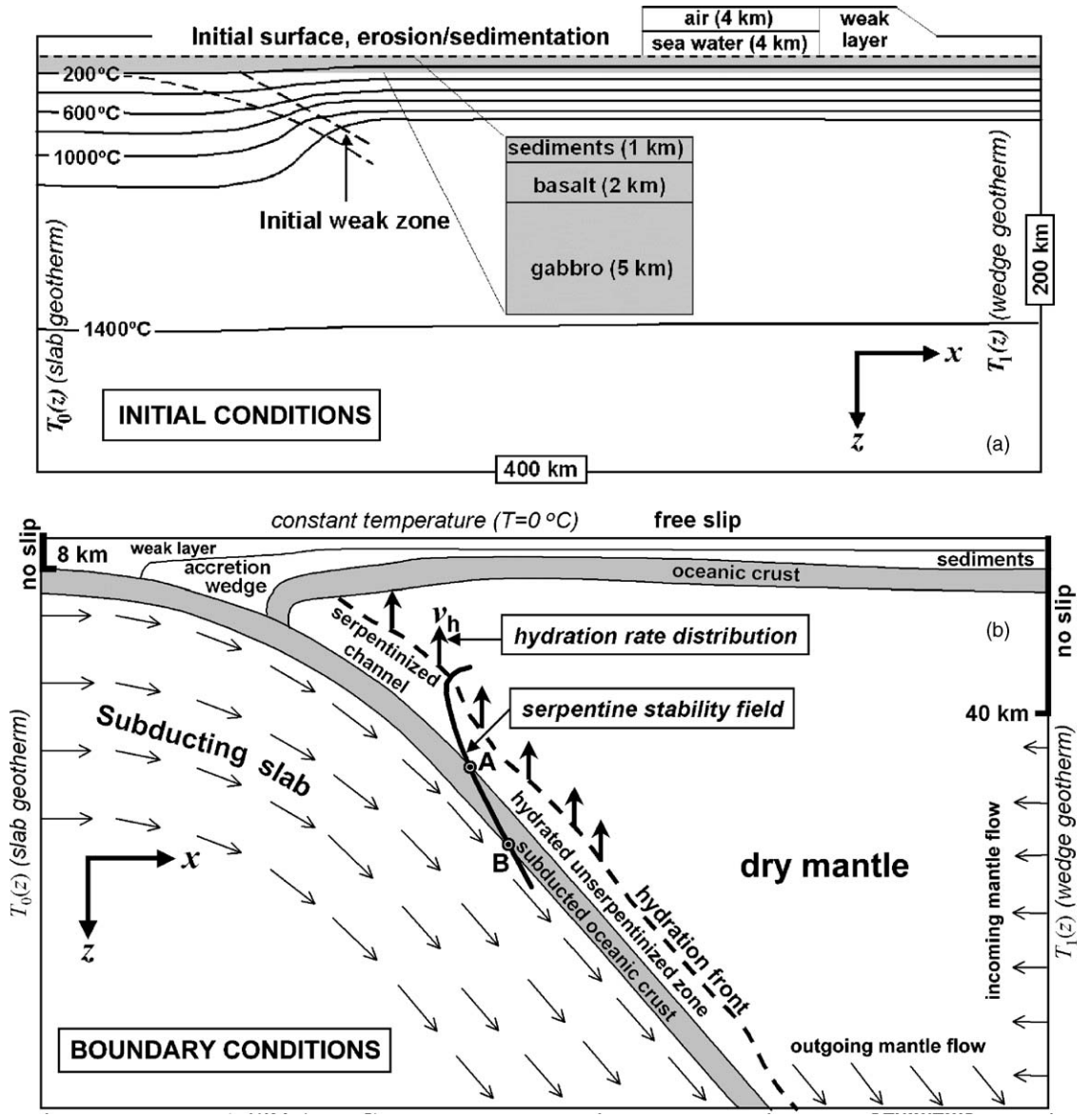

Fig. 2. Numerical upper-mantle model (Gerya and Yuen, 2003a) used in our two-dimensional numerical experiments. Initial conditions (a) for calculation are taken as follows: the initial position of the subduction zone is prescribed by a weak, 6 km-thick, hydrated peridotite layer; initial temperature field in subducting plate is defined by an oceanic geotherm $T_0(z)$ with a specified age; initial temperature distribution in overriding plate $T_1(z)$ corresponds to equilibrium thermal profile with 0 °C at surface and 1350 °C at 32 km depth; initial structure of 8 km-thick oceanic crust is taken as follows (from top to bottom): sedimentary rocks = 1 km, basaltic layer = 2 km, gabbroic layer = 5 km. Boundary conditions and hydration model (b) are shown for the intermediate stage of calculation with well-developed hydrated mantle zone. A and B are intersection points of serpentine stability field (Table 3, note) with respectively upper and lower surface of the oceanic crust. Further details of model design and limitations are given in our previous paper (Gerya and Yuen, 2003a).

is assumed to be negligible compared to the amount of water stored in hydrous phases and melts.

3. Thermomechanical model

We employ a 2D numerical thermomechanical model (Fig. 2) with a kinematically prescribed velocity of the subducting plate (Gerya and Yuen, 2003a). The boundary conditions account for incoming and outgoing asthenospheric flow under the overriding plate. The top surface of the oceanic crust is calculated dynamically as a free surface by using an 8 km-thick hydrosphere with low viscosity (10^{18} Pa s) and density (1 kg/m^3 for the atmosphere, 1000 kg/m^3 for seawater). The interface between this weak layer and the top of the oceanic crust deforms spontaneously and is treated as an erosion/sedimentation surface (Gerya and Yuen, 2003a). Accounting for the thermal and density effects of phase transformations poses a significant challenge (Bittner and Schmeling, 1995; Barboza and Bergantz, 1997; Vasilyev et al., 2004) because abrupt changes associated with the appearance of a phase are difficult to handle numerically, particularly in the continuity condition. To overcome these difficulties, we employ the incompressible fluid approximation for the continuity equation and numerical smoothing of thermal and density effects due to phase changes for the momentum and temperature equation (Gerya et al., 2004b). Transport and physical properties are then computed by finite differences and a marker-in-cell technique (Gerya et al., 2000; Gerya and Yuen, 2003b).

The momentum, continuity, and thermal equations for the two-dimensional creeping-flow equations, accounting for both thermal and chemical buoyancy, are solved using the I2VIS code (Gerya and Yuen, 2003b) based on conservative finite differences and a nondiffusive-marker-in-cell technique. The thermal equation is formulated as (Gerya and Yuen, 2003b)

$$\rho C_p \left(\frac{\mathrm{D}T}{\mathrm{D}t}\right) = -\frac{\partial q_x}{\partial x} - \frac{\partial q_z}{\partial z} + H_\mathrm{r} + H_\mathrm{a} + H_\mathrm{S} + H_\mathrm{L},$$

$$q_x = -k(T,C)\frac{\partial T}{\partial x}, \quad q_z = -k(T,C)\frac{\partial T}{\partial z},$$

$$H_\mathrm{a} = T\alpha\frac{\mathrm{D}P}{\mathrm{D}t}, \quad H_\mathrm{S} = \sigma_{xx}\dot{\varepsilon}_{xx} + \sigma_{zz}\dot{\varepsilon}_{zz} + 2\sigma_{xz}\dot{\varepsilon}_{xz}, \quad (4)$$

where D/Dt is the substantive time derivative; x and z denote, respectively, the horizontal and vertical coordinates; σ_{xx}, σ_{xz}, σ_{zz} the components of the deviatoric stress tensor; $\dot{\varepsilon}_{xx}$, $\dot{\varepsilon}_{xz}$, $\dot{\varepsilon}_{zz}$ the components of the strain rate tensor in; P the pressure; T the temperature; q_x and q_z the heat fluxes; ρ the density; g the gravitational acceleration; $k(T, C)$ the thermal conductivity, a function of composition and temperature (Table 2, e.g., Thompson and Connolly, 1995); C_p the isobaric heat capacity; H_r, H_a, H_S and H_L denote, respectively, radioactive, adiabatic, shear and latent heat production.

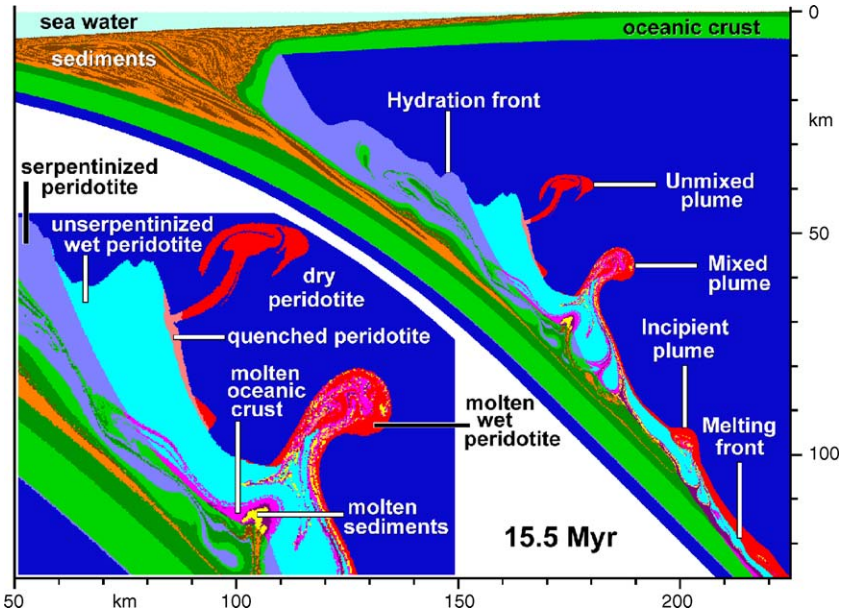

Fig. 3. Development of unmixed and mixed plumes due to hydration of the mantle wedge by fluids released from the slab. Results from high-resolution numerical model (Model 10 in Table 4) are shown. The corrugations along the hydration front reflect dynamics of slab dehydration (Eq. (1)–(3)). Zoomed area shows lithological structures of mixed and unmixed plumes.

Table 4
Parameters of selected numerical experiments

Model	Slab rate (cm/year)	Slab age (Myear)	η_{serp} (Pa s)	Grid step (km)[a]	Erosion, sedimentation rate (mm/year)	Plumes initiation			
						Time (Myear)	Length of subduction (km)	Depth (km)	Rocks[b]
1. (04_19_01H)	1	40	10^{19}	2	0.3	19.1	191	160	p
						30.2	302	80	c + p
						56.4	564	192	p
						68.2	682	185	c + p
						77.4	774	198	c ≈ p
2. (04_19_05H)	5	40	10^{19}	2	0.3	2.9	145	91	p
						5.4	270	57	p
						6.0	300	65	p
						6.0	300	95	c + p
						7.8	390	112	c + p
						12.8	640	116	p
3. (04_18_05H)	5	40	10^{18}	2	0.3	2.9	145	89	p
						5.4	270	59	c ≈ p
						5.4	270	78	c ≪ p
						12.2	610	119	p
						13.1	655	87	c + p
						14.6	730	100	c + p
4. (04_18_03)[c]	3	40	10^{18}	2	0.3	5.7	171	81	p
						9.3	279	178	c ≈ p
						11.5	345	193	c + p
						38.6	1158	200	c ≪ p
5. (04_19_03S)[c]	3	40	10^{19}	2	1	5.2	156	93	p
						19.5	585	110	p
						38.7	1161	78	p
6. (04_18_02HR)	2	40	10^{18}	1	0.3	3.8	76	63	p
						8.6	172	50	
						11.8	236	197	c + p
						12.5	250	72	c + p
						15.5	310	112	c + p
						20.3	406	118	p
						26.6	532	200	p
7. (02_18_02)[c]	2	20	10^{18}	2	0.3	11.5	230	65	p
						13.6	272	72	c ≈ p
						19.3	386	87	c ≈ p
						45.0	900	150	c ≪ p
8. (10_18_02)[c]	2	100	10^{18}	2	0.3	8.5	170	90	p
						13.0	260	175	c ≪ p
						30.2	604	100	c ≪ p
						37.2	744	200	c + p
9. MAXA)[c,d]	5	40	10^{19}	2	0.3	3.3	163	76	p
						16.4	822	140	c + p
10. (HIGH)	2	40	10^{19}	1	0.3	3.9	78	58	p
						6.6	132	58	p
						15.2	304	67	c + p
						47.7	934	90	c + p

[a] Grid step: 1 km, 401 × 201 nodes, ~8 million markers; 2 km, 201 × 101 nodes, ~0.5 million markers.

[b] Rock abbreviations: p = peridotite, c = subducted crustal rocks (sediments, oceanic crust).

[c] Simplified hydration model (Gerya and Yuen, 2003a): subducted oceanic crust dehydration $v_{h(x)} = 0.05 v_{subd}$ when $0 < x < x_A$; serpentine dehydration in the slab $v_{h(x)} = K v_{subd}$, when $x_A < x < x_B$; no deep dehydration of the slab $v_{h(x)} = 0$ when $x > x_B$, where $v_{h(x)}$ is the substantive hydration rate along the hydration front (Eq. (1)) as the function of horizontal distance x, x_A and x_B are imposed limits for the interval of serpentine dehydration in the slab (Fig. 2, Table 3), K is mantle hydration constant ($K = 0.5$ for the mantle below wet solidus, $K = 0.15$ for the mantle above wet solidus, see Section 4).

[d] Simplified density model (Gerya and Yuen, 2003a).

The effective creep viscosities of solid rocks are represented as a function of temperature and stress by experimentally determined flow laws (Table 3). The consequences of variation in rheology on subduction zone dynamics are discussed by (Gerya and Stoeckhert, 2002, 2006). Partially molten rocks are assigned a reduced effective viscosity of 10^{17} Pa s which represent upper bound for partially molten systems (10^{14}–10^{17} Pa s, e.g., Pinkerton and Stevenson, 1992) but still much lower then that of solid rocks (10^{18}–10^{25} Pa s).

A total of 102 numerical experiments were done (partially summarized in Table 4) as a function of subduction rate (1–5 cm/year) and slab age (20–100 Myear). The use of a large number of markers ($0.5 - 8.0 \times 10^6$) allows spatial resolution approaching 100 m (cf. Fig. 3, Models, 6, 10 in Table 4, see also Rudolph et al., 2004).

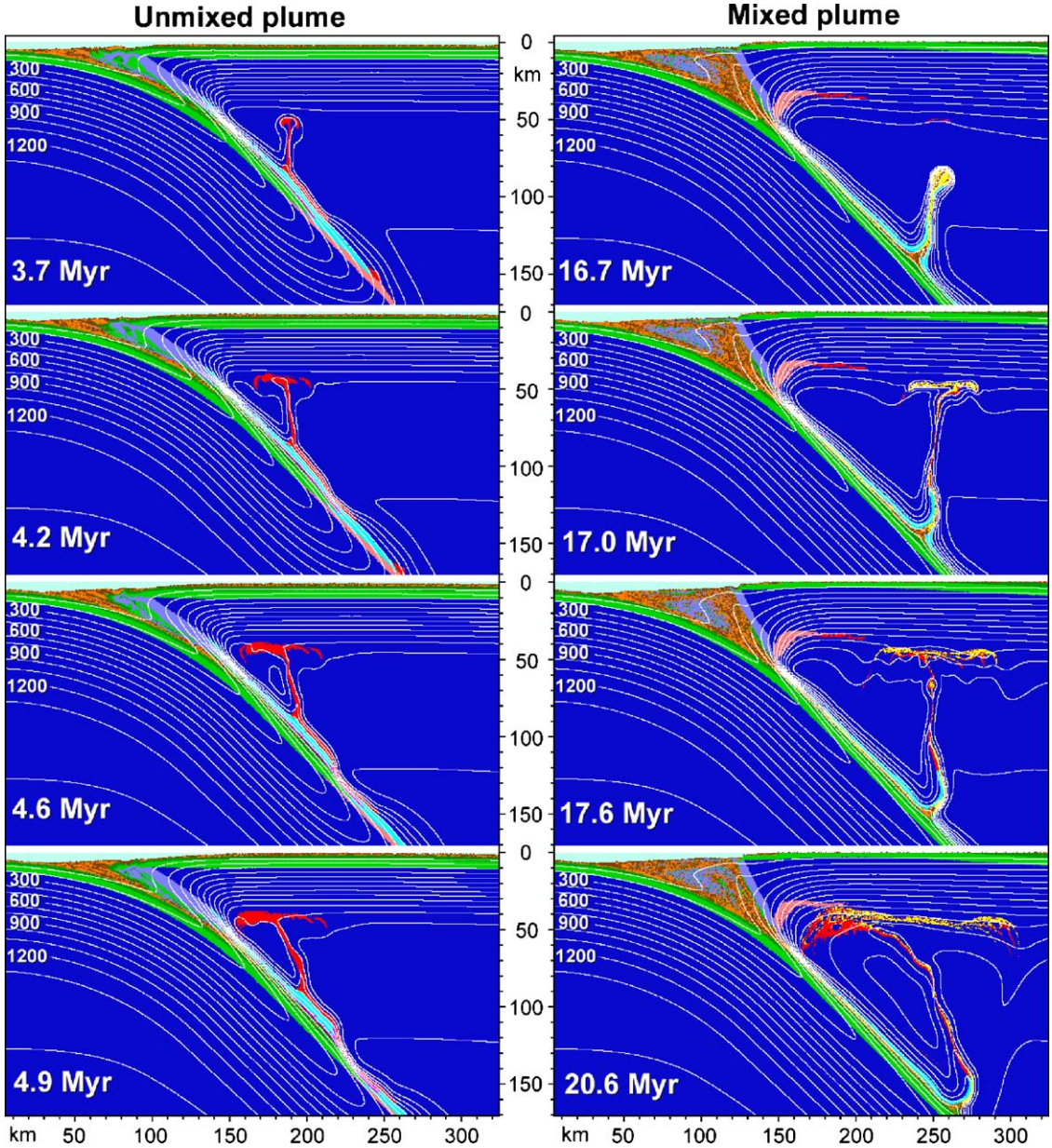

Fig. 4. Evolution of lithological field and isotherms (white lines labeled in °C) during the propagation of unmixed (left column) and mixed (right column) plumes. Results from medium-resolution numerical model (Model 9 in Table 4) are shown. Color code is the same as in Fig. 3.

4. Dynamics of thermal–chemical plumes

In this section, we focus on plumes that develop in the numerical experiments above the descending lithosphere. Plume development is enhanced by hydration of the mantle wedge by volatiles released from the subducted slab (e.g., Gerya et al., 2002). At asthenospheric depths, corrugations along the hydration front (Fig. 3) that arise through the dynamics of slab dehydration (Eqs. (1)–(3)), provide perturbations that excite the Rayleigh–Taylor instabilities from which the plumes develop (Figs. 3 and 4). The computed widths of the hydrated zone in the mantle wedge vary from several kilometers to a few tens of kilometers (Fig. 3) as consistent with seismic data (Bostock et al., 2002).

Systematic study shows that the length of subduction after which plumes first initiate decreases with: (i) increasing subduction rate (cf. Models 1 and 2 in Table 4), (ii) increasing amount of subducted sediments due to the increase in erosion/sedimentation rate (cf.

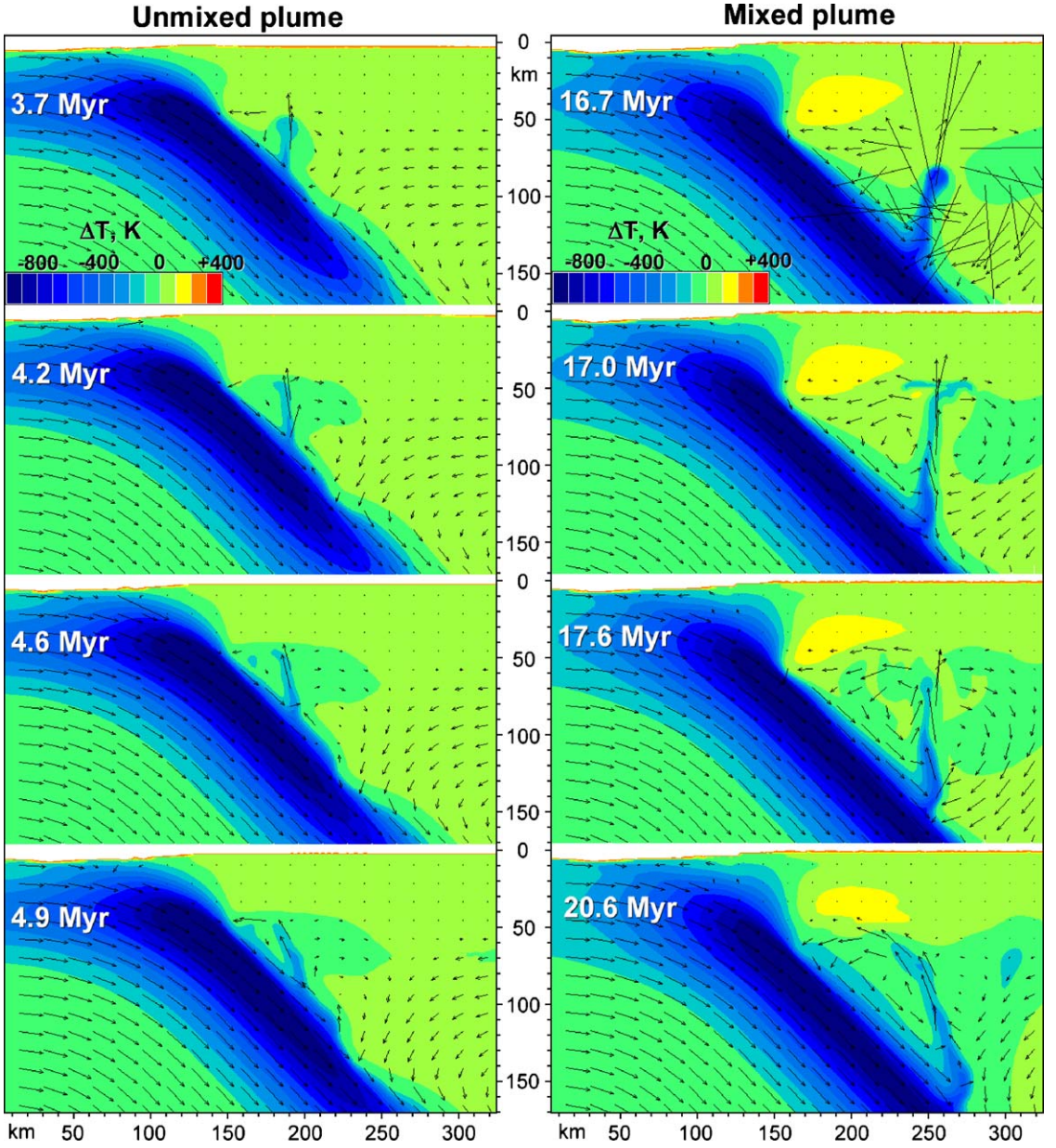

Fig. 5. Evolution of temperature (color code) and movement rate (arrows) computed for the model shown in Fig. 4 (Model 9 in Table 4). Variations in temperature are computed relative to the vertical profile in the mantle wedge at $x = 350$ km.

Models 4 and 5 in Table 4), and (iii) increasing slab age (cf. Models 7 and 8 in Table 4). Variation in viscosity of serpentinized mantle (Fig. 3) does not significantly affect the onset of plume initiation but does affect plume dynamics at greater depth (cf. Models 2 and 3, Models 6 and 10 in Table 4). Initiation of plumes at later stages of subduction are affected by several factors which cannot always be isolated by varying model parameters. Most important among these factors are: (i) changes in effective viscosities due to P–T-strain rate dependent rheology, (ii) changes in density due to mineral reactions including hydration and melting, (iii) changes of plume growth rate due to the Rayleigh–Taylor instability, (iv) movement of the subducting plate and (v) circulation of asthenospheric mantle in the wedge as affected by propagation of early formed plumes.

In contrast to models that did not account for the effects of metamorphic reactions and melting, the present models show two distinct sources for Rayleigh–Taylor instabilities may initiate plumes. As in

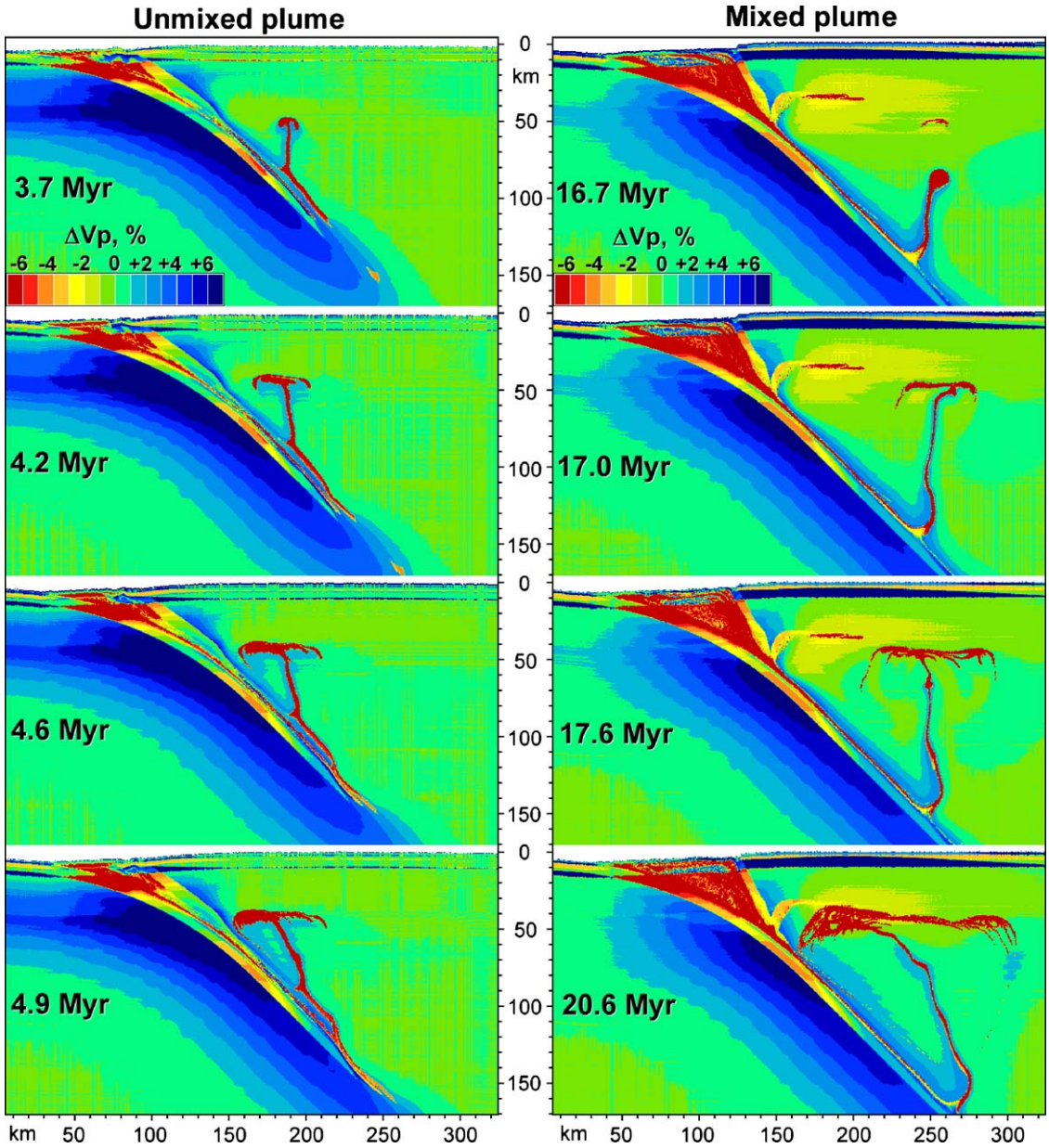

Fig. 6. Evolution of compression wave seismic velocity (v_p) field computed for the model shown in Fig. 4 (Model 9 in Table 4). Variations in v_p are computed relative to the vertical profile in the mantle wedge at $x = 350$ km.

the models of Gerya and Yuen (2003a), hydrous minerals and melts within the subducted slab form a source from which plumes are expected to carry a strong crustal signature. Such plumes consist of partially molten mantle and crustal rocks mixed on length-scales of 1–100 m (Rudolph et al., 2004). The second source originates from the upward propogating hydration front that forms within the mantle wedge as a consequence of slab dehydration (Figs. 3 and 4). Once physical conditions behind this front reach those of mantle melting (Table 3) a layer of partially molten mantle forms behind the hydration front. The lower boundary of this partially molten layer (melting front, Fig. 3) varies depending on the temperature of the wet solidus at a given depth, but is subparallel to, and a few kilometers above, the slab (Fig. 3). Upward propagation rates for plumes (Fig. 5) from either source are of the order 0.01–1 m/year; thus the plumes offer a mechanism by which thousands of cubic kilometers of material can be transported through the mantle wedge. The two sources generate distinct types of plumes: mixed

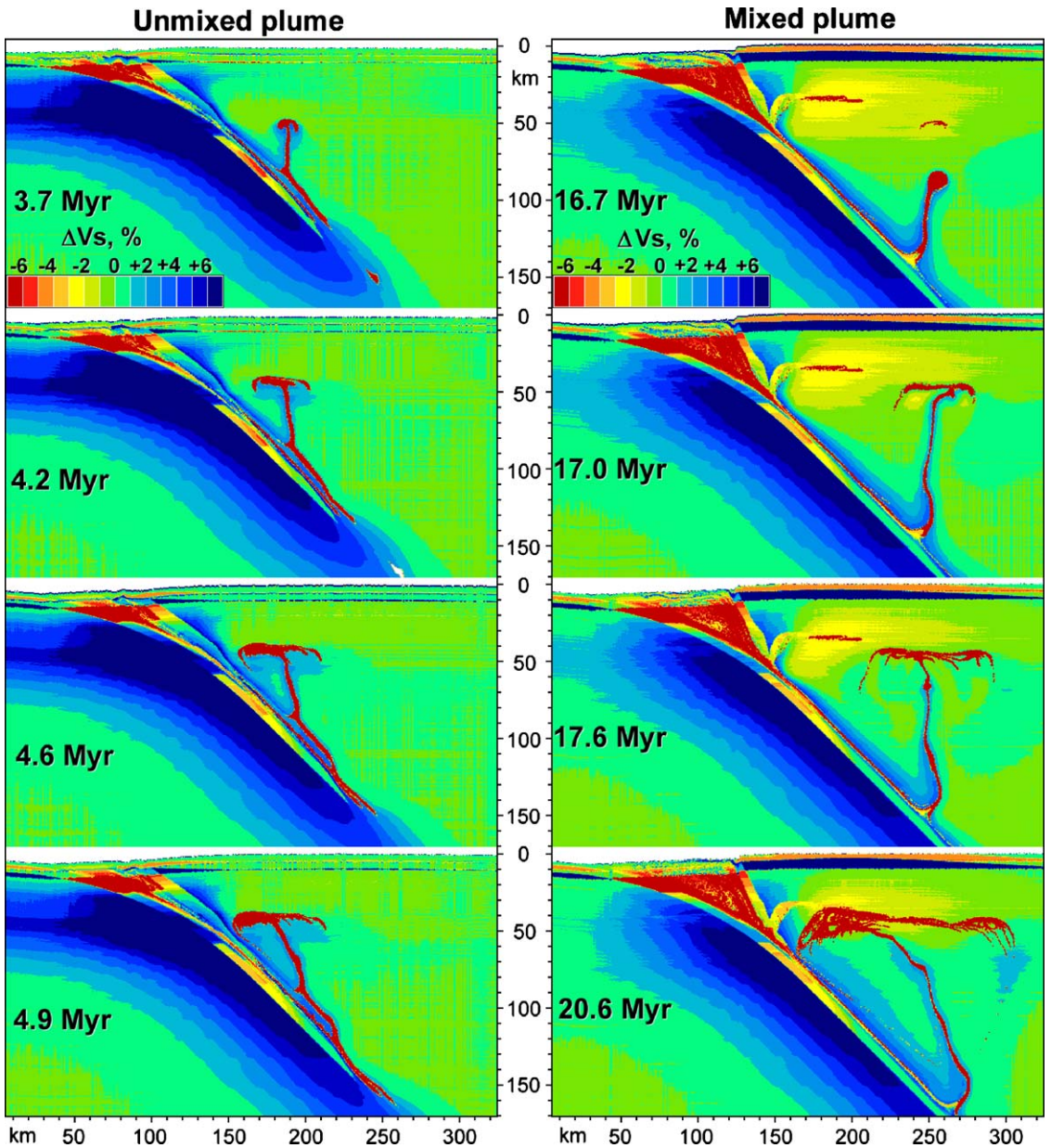

Fig. 7. Evolution of shear wave seismic velocity (v_s) field computed for the model shown in Fig. 4 (Model 9 in Table 4). Variations in v_s are computed relative to the vertical profile in the mantle wedge at $x = 350$ km.

plumes (Figs. 3 and 4, right column) consist of partially molten crustal and mantle rocks; and unmixed plumes (Figs. 3 and 4, left column) consist of partially molten mantle. This distinction leads us to hypothesize that arc magmas with crustal melt geochemical signatures are derived from mixed plumes, whereas primitive magmas with slab fluid signatures derive from unmixed plumes. The time and depth of generation for mixed and unmixed plumes does not vary systematically (Table 4). However, at the initial stages of subduction unmixed plumes are prevalent and form nearer to the trench than is generally the case for mixed plumes (Figs. 3 and 4).

5. Synthetic seismic tomographic images

The volatiles/melts and temperature fields (cf. Figs. 4 and 5) resulting from plume propagation compete in shaping the seismic structure of the mantle wedge. The relative importance of these factors causes the seismic signal to change during plume propagation. Positive

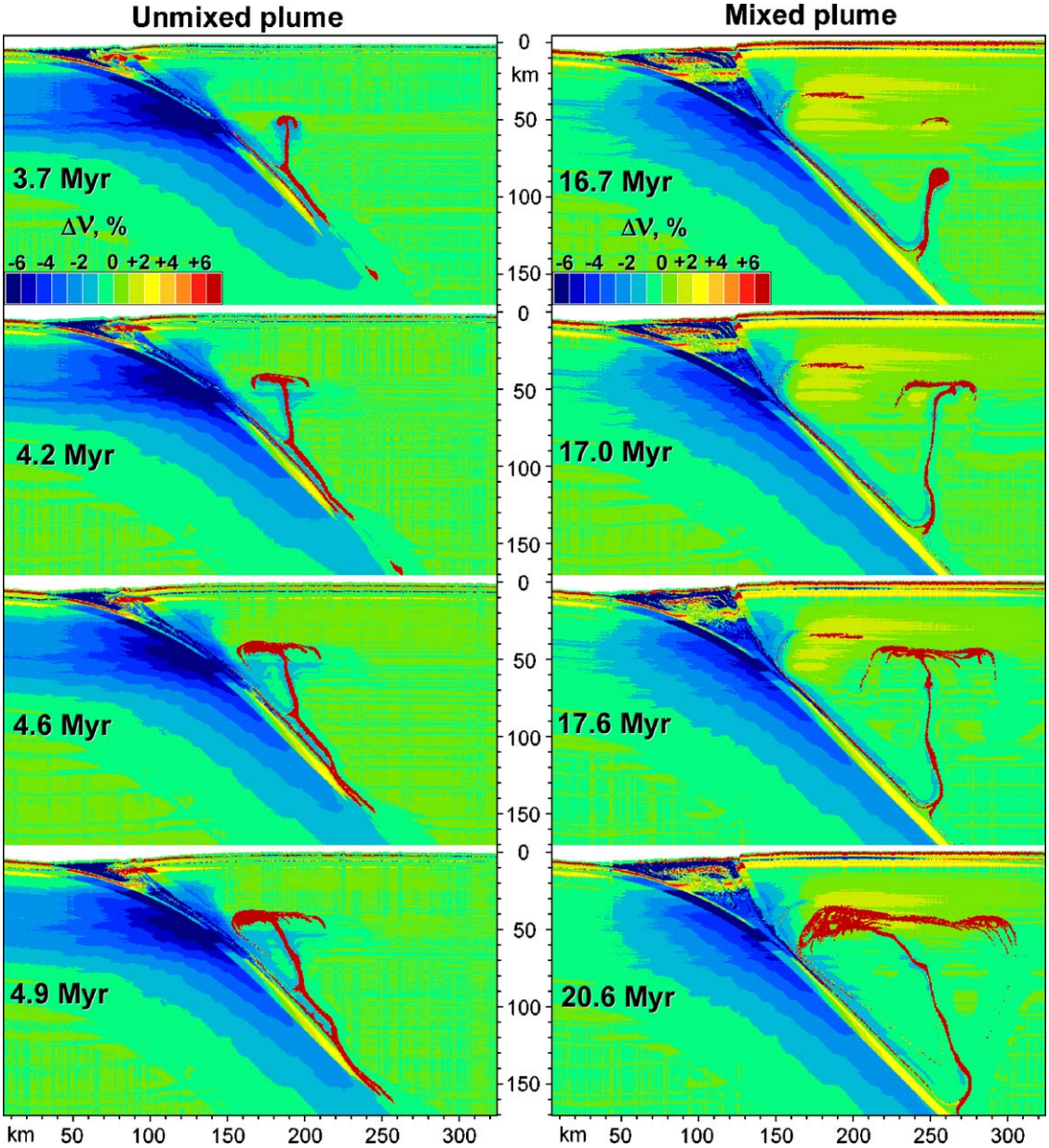

Fig. 8. Evolution of Poisson ratio (ν) field computed for the model shown in Fig. 4 (Model 9 in Table 4). Variations in Poisson ratio are computed relative to the vertical profile in the mantle wedge at $x = 350$ km.

anomalies are characteristic of the roots of plumes (Figs. 5 and 6), whereas negative seismic anomalies are common at shallower depth due both to the presence of partially molten rocks composing plume heads and the formation of 30–50 km wide flattened melting regions that form beneath volcanic arcs (e.g., Fig. 4, at 20.6 Myear) as a consequence of cold wet plumes (Gerya et al., 2004a). The negative velocity anomalies are generally greater then 10% and stronger than those associated with variations in temperature within the mantle wedge (<6%, cf. Figs. 5–7). Poisson ratio anomalies are even more pronounced: the positive anomaly for molten plumes often exceeds 20% and is several times larger than that for variations caused by temperature. For comparison, the core of the subducting slab which is 500–1000 K colder then the wedge (Fig. 5) is manifest by a Poisson ratio anomaly of only 2–5% (Fig. 8).

6. Discussion and conclusions

The advantage of our coupled petrological–thermomechanical model is that it naturally specifies many rock properties that vary as a function of pressures and temperature, e.g., density, heat capacity, thermal expansion, latent heat, and water content. These properties are not the subject of arbitrary choice, but rather are computed using natural rock compositions (Table 1) and an extensively tested thermodynamic data base (Holland and Powell, 1998, Table 2). The parameters in this data base are subject to strong autocorrelation and therefore cannot be viewed as independently variable. Thus, the number of independently variable model parameters in our model is no greater than in conventional thermomechanical subduction zone models; these parameters include subduction rate, lithology, slab age and rheology. These computed rock properties from the petrological model feedback to the thermomechanical model, thereby assuring internally consistency of the overall solution. Models inevitably represent a simplification and may entirely neglect important natural processes, in this regard areas that must be explored more thoroughly are: the consequences of variations in the rheology and structures of the subducting slab and overriding plate; effects of mineral reaction kinetics; and multi-phase flow models pertinent to melt extraction and magmatic arc growth.

Our models reveal that two distinct types of plumes (mixed and unmixed) form in the mantle wedge. These distinct plume types can explain the presence of different magmas in volcanic arcs (e.g., Stern, 2002): magmas with distinct crustal signatures (e.g., adakites) and primitive magmas from peridotitic source (e.g., arc tholeiites). Thermal zoning inside rapidly rising unmixed cold plumes can result in transitory bimodal magmatism because of both the compositional and the thermal zoning of these structures (Fig. 4, left column), which would generate basalts from its water-depleted, hot rinds, and boninites from its water-enriched, cooler interiors (Tamura, 1994; Gerya et al., 2004a). Rates of plume propagation vary between several centimeters to meters per year (Gerya and Yuen, 2003a; Gerya et al., 2004a) corresponding to 0.1–3 Myear transfer time through the athenospheric portion of the mantle wedge (Fig. 4). This is consistent with U–Th isotope measurements from island arc magmas that suggest short transfer times for fluids (0.03–0.12 Myear) and slab-derived melts (several Myear) (Hawkesworth et al., 1997). Intense melting of subducted sediments and oceanic crust in the mixed plumes occurs at the temperature above 650 °C (Fig. 4, 16.7 Myear) after penetration of these structures into the hot portion of the mantle wedge. This behavior agrees well with geochemical models suggesting sediment melting beneath the arc, behavior which is otherwise difficult to reconcile with low slab surface temperature inferred from thermal models for subduction zones as discussed by George et al. (2003).

The models presented here are two-dimensional; thus the plume dynamics correspond to development of planar, sheet-like instabilities. An important question, therefore, concerns implications of our study for the initiation and propagation of cold plumes in three-dimensions. According to numerical studies of diapirism (Kaus and Podladchikov, 2001) both finger-like and sheet-like diapiric structures are stable in 3D and have similar initial growth rates. Therefore, it is reasonable to expect that the dynamics of plume initiation dynamics established in our study are applicable for 3D subduction process where both sheet-like and finger-like (e.g., Gerya and Yuen, 2003a) structures can form.

The role of volatiles in subduction dynamics has received recent attention (e.g., Regenauer-Lieb et al., 2001). There may be several competing mechanisms of fluid/melt transport in subduction zones including hydrofracture (e.g., Clemens and Mawer, 1992), diffusion (e.g., Scambelluri and Philippot, 2001), porous flow (e.g., Scott and Stevenson, 1986; Connolly and Podladchikov, 1998; Vasilyev et al., 1998) reactive flow (e.g., Spiegelman and Kelemen, 2003) and diapirism (e.g., Hall and Kincaid, 2001; Gerya and Yuen, 2003a; Manea et al., 2005). Since the upward propagation rate of partially molten diapirs can reach several meters per year and the volume of these finger-like and sheet-like structures can reach thousands of cubic kilometers, we hypothesize that the transport of hydrated partially

molten rock is efficient in the hot asthenospheric part of the mantle wedge (e.g., Gerya and Yuen, 2003a; Gerya et al., 2004a). In the Earth's crust similar processes are responsible for the formation of partially molten cupola and diapiric structures (e.g., Ramberg, 1981; Bittner and Schmeling, 1995) including "cold diapirs" from Bushveld complex (Gerya et al., 2003) that are similar to the phenomena investigated here. Other mechanisms, such as hydrofracture, diffusion and porous flow, may dominate in relatively cold areas of subduction zones, for example within and immediately above the slab (e.g., Scambelluri and Philippot, 2001; Davies and Stevenson, 1992) and lithospheric portion of the mantle wedge (e.g., Peacock, 1987).

An important related issue concerns possible role of melt segregation from partially molten plumes. It is assumed in our model that the melt does not escape quickly, an assumption that increases plume buoyancy and the resulting transport velocities. This assumption cannot be strictly valid, since arc volcanoes attest to melt segregation. In this regard, the validity of the models hinges on the depths at which segregation becomes significant. Thus, the models are valid if segregation occurs in the flattened partially molten region formed below the arc (Fig. 4, 20.6 Myear). Several factors may hinder early melt segregation in cold plumes. In the initial stages of plume growth melt segregation must compete with melt production induced by volatile fluxes from the slab. During plume upwelling melt segregation competes with melt production due to conductive and shear heating and decompression melting (Gerya and Yuen, 2003a). In contrast, once plumes begin to stagnate beneath the arc there is more time for melt segregation. At this late stage melt segregation would decrease the buoyancy of partially molten rocks underplating volcanic arcs, an effect that might trigger downwelling.

Seismic tomography (Smith et al., 2001; Zhao, 2001; Zhao et al., 1992) can shed light on the nature of plumes and/or diapiric structures rising from the subducted slab. The tomographic image of the subduction zone beneath Japan (after Zhao (2001), Fig. 9) shows how such images constrain the path of rising structures. The thermal–chemical plumes studied here are dynamical structures such that the positive seismic anomalies associated with plume initiation evolve to negative anomalies at shallower depth (Fig. 6) due to the conductive and shear heating and decompression melting (Gerya and Yuen, 2003a). The model tomographic variations are consistent (cf. Figs. 6 and 9) with strong seismic anomalies detected in mantle wedges (e.g., Zhao, 2001). Other models proposed to explain these anomalies (e.g., Honda and Saito, 2003; Honda et al., 2002) based entirely on

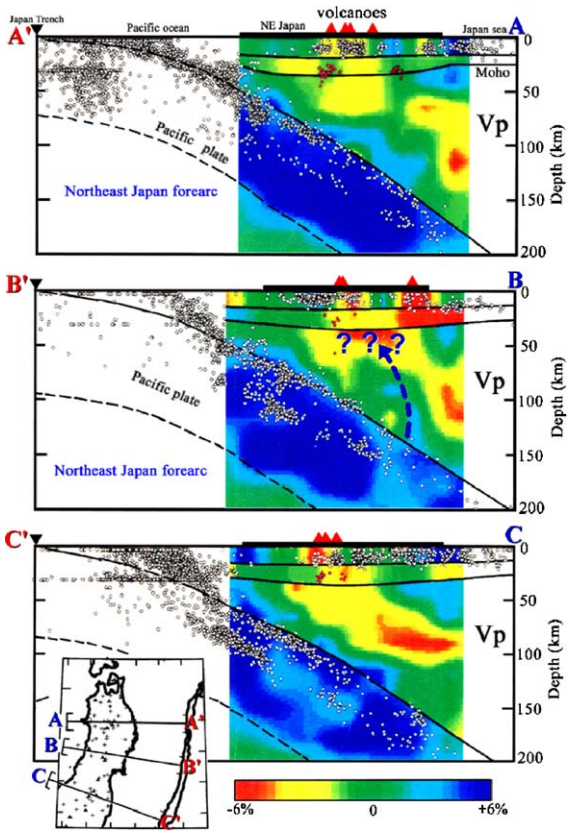

Fig. 9. Tomographic structure of the mantle wedge beneath Japan (modified after Zhao, 2001). Blue arrow in the middle section shows presumed trace of cold plume propagation below the volcanic arc marked by positive v_p anomaly. Blue question marks denote negative compressional wave seismic velocity anomaly which may correspond to the partially molten head of cold plume (cf. Figs. 4–6). Original orientation of vertical sections is mirrored to facilitate comparison with numerical modeling results. (For interpretation of the references to color in this figure legend, the reader is referred to the web version of the article.)

thermal variations, are unable to explain such strong seismic anomalies. In particular, v_p seismic anomalies of 5–6% relative (Fig. 9) are detected in mantle wedges (e.g., Zhao, 2001). To explain such anomalies purely by thermal effects require local temperature variations of 500–600 K (cf. Figs. 5 and 6) in the asthenospheric portion of the mantle wedge. Variations of this magnitude are significantly lager than anticipated by thermal models (e.g., Honda and Saito, 2003; Honda et al., 2002).

Our high-resolution tomographic images can be employed for testing out various seismic nonlinear inversion algorithms (Bijwaard and Spakman, 1999) and assess the accuracy of ray-tracing algorithms on realistic structures (Gorbatov et al., 2000), which have been obtained from realistic and high-resolution

geodynamical modeling and include both thermal and compositional contributions to the seismic anomalies.

Acknowledgments

This work was supported by ETH Research Grants TH-12/04-1, TH-12/05-3, by RFBR grant #03-05-64633, by the RF President Program "Leading Scientific School of Russia" (grant #03.5.1645) to T.V.G., by CSEDI and ITR programs of the National Science Fondation. Dapeng Zhao is thanked for sending us the figure with tomographic model under Japan. We also thank Satoru Honda for serious discussion. Constructive reviews by two anonymous reviewers and editorial handling by G. Schubert are appreciated.

References

Barboza, S.A., Bergantz, G.W., 1997. Melt productivity and rheology: complementary influences on the progress of melting. Numeric. Heat Transfer Part A-Appl. 31, 375–392.

Behn, M.D., Kelemen, P.B., 2003. Relationship between seismic P-wave velocity and the composition of anhydrous igneous and meta-igneous rocks. Geochem. Geophys. Geosyst. 4, art. no. 1041.

Bijwaard, H., Spakman, W., 1999. Fast kinematic ray tracing of first- and later-arriving global seismic phases. Geophys. J. Int. 139, 359–369.

Bina, C.R., Helffrich, G., 1992. Calculation of elastic properties from thermodynamic equation of state principles. Annu. Rev. Earth Planet. Sci. 20, 527–552.

Bittner, D., Schmeling, H., 1995. Numerical modeling of melting processes and Induced diapirism in the lower crust. Geophys. J. Int. 123, 59–70.

Bostock, M.G., Hyndman, R.D., Rondenay, S., Peacock, S.M., 2002. An inverted continental Moho and serpentinization of the forearc mantle. Nature 417, 536–538.

Carlson, R.L., 2003. Bound water content of the lower oceanic crust estimated from modal analyses and seismic velocities of oceanic diabase and gabbro. Geophys. Res. Lett. 30, art. no. 2142.

Carlson, R.L., Miller, D.J., 2003. Mantle wedge water contents estimated from seismic velocities in partially serpentinized peridotites. Geophys. Res. Lett. 30, art. no. 1250.

Clauser, C., Huenges, E., 1995. Thermal conductivity of rocks and minerals. In: Ahrens, T.J. (Ed.), Rock Physics and Phase Relations. American Geophysical Union, Washington, DC, pp. 105–126.

Clemens, J.D., Mawer, C.K., 1992. Granitic magma transport by fracture propagation. Tectonophysics 204, 339–360.

Connolly, J.A.D., 2005. Computation of phase equilibria by linear programming: a tool for geodynamic modeling and an application to subduction zone decarbonation. Earth Planet. Sci. Lett. 236, 524–541.

Connolly, J.A.D., Kerrick, D.M., 2002. Metamorphic controls on seismic velocity of subducted oceanic crust at 100–250 km depth. Earth Planet. Sci. Lett. 204, 61–74.

Connolly, J.A.D., Podladchikov, Y.Y., 1998. Compaction-driven fluid flow in viscoelastic rock. Geodinam. Acta 11, 55–84.

Davies, H.J., Stevenson, D.J., 1992. Physical model of source region of subduction zone volcanics. J. Geophys. Res. 97, 2037–2070.

Davies, J.H., 1999. The role of hydraulic fractures in generating intermediate depth earthquakes and subduction zone magmatism. Nature 398, 142–145.

George, R., Turner, S., Hawkesworth, C., Morris, J., Nye, C., Ryan, J., Zheng, S.-H., 2003. Melting processes and fluid and sediment transport rates along the Alaska-Aleutian arc from an integrated U-Th-Ra-Be isotope study. J. Geophys. Res., 108, doi:10.1029/2002JB001916.

Gerya, T.V., Stoeckhert, B., 2002. Exhumation rates of high pressure metamorphic rocks in subduction channels: the effect of Rheology. Geophys. Res. Lett. 29, art. no. 1261.

Gerya, T.V., Stoeckhert, B., 2006. Two dimensional numerical modeling of tectonic and metamorphic histories at active continental margins. Int. J. Earth Sci. 95, 250–274.

Gerya, T.V., Yuen, D.A., 2003a. Rayleigh-Taylor instabilities from hydration and melting propel 'cold plumes' at subduction zones. Earth Planet. Sci. Lett. 212, 47–62.

Gerya, T.V., Yuen, D.A., 2003b. Characteristics-based marker-in-cell method with conservative finite-differences schemes for modeling geological flows with strongly variable transport properties. Phys. Earth Planet. Interiors 140, 295–320.

Gerya, T.V., Perchuk, L.L., van Reenen, D.D., Smit, C.A., 2000. Two-dimensional numerical modeling of pressure-temperature-time paths for the exhumation of some granulite facies terrains in the Precambrian. J. Geodyn. 30, 17–35.

Gerya, T.V., Stoeckhert, B., Perchuk, A.L., 2002. Exhumation of high-pressure metamorphic rocks in a subduction channel: a numerical simulation. Tectonics 21, 6-1–6-19.

Gerya, T.V., Uken, R., Reinhardt, J., Watkeys, M.K., Maresch, W.V., Clarke, B.M., 2003. Cold fingers in a hot magma: numerical modeling of diapirs in the Bushveld Complex, South Africa. Geology 31, 753–756.

Gerya, T.V., Yuen, D.A., Sevre, E.O.D., 2004a. Dynamical causes for incipient magma chambers above slabs. Geology 32, 89–92.

Gerya, T.V., Perchuk, L.L., Maresch, W.V., Willner, A.P., 2004b. Inherent gravitational instability of hot continental crust: implication for doming and diapirism in granulite facies terrains. In: Whitney, D., Teyssier, C., Siddoway, C.S. (Eds.), Gneiss Domes in Orogeny. GSA Special Paper, pp. 117–127.

Ghiorso, M.S., Hirschmann, M.M., Reiners, P.W., Kress, V.C., 2002. The pMELTS: a revision of MELTS for improved calculation of phase relations and major element partitioning related to partial melting of the mantle to 3 GPa. Geochem. Geophys. Geosyst. 3, art. no. 1030.

Gorbatov, A., Widiyantoro, S., Fukao, Y., Gordeev, E., 2000. Signature of remnant slabs in the North Pacific from P-wave tomography. Geophys. J. Int. 142, 27–36.

Hacker, B.R., Abers, G.A., 2004. Subduction Factory 3: an excel worksheet and macro for calculating the densities, seismic wave speeds, and H_2O contents of minerals and rocks at pressure and temperature. Geochem. Geophys. Geosyst., 5.

Hall, P.S., Kincaid, C., 2001. Diapiric flow at subduction zones: a recipe for rapid transport. Science 292, 2472–2475.

Hart, S.R., Zindler, A., 1986. In search of a bulk-earth composition. Chem. Geol. 57, 247–267.

Hawkesworth, C.J., Turner, S.P., McDermott, F., Peate, D.W., van-Calsteren, P., 1997. U–Th isotopes in arc magmas: Implications for element transfer from the subducted crust. Science 276, 551–555.

Holland, T., Baker, J., Powell, R., 1998. Mixing properties and activity-composition relationships of chlorites in the system MgO-FeO-Al_2O_3-SiO_2-H_2O. Euro. J. Miner. 10, 395–406.

Holland, T., Powell, R., 1996. Thermodynamics of order-disorder in minerals. 2. Symmetric formalism applied to solid solutions. Am. Miner. 81, 1425–1437.

Holland, T.J.B., Powell, R., 1998. An internally consistent thermodynamic data set for phases of petrological interest. J. Metamorphic Geol. 16, 309–343.

Honda, S., Saito, M., 2003. Small-scale convection under the back-arc occurring in the low viscosity wedge. Earth Planet. Sci. Lett. 216, 703–715.

Honda, S., Saito, M., Nakakuki, T., 2002. Possible existence of small-scale convection under the back arc. Geophys. Res. Lett. 29, art. no. 2043.

Jung, H., Karato, S., 2001. Water-induced fabric transitions in olivine. Science 293, 1460–1463.

Kaus, B.J.P., Podladchikov, Y.Y., 2001. Forward and reverse modeling of the three-dimensional viscous Rayleigh–Taylor instability. Geophys. Res. Lett. 28, 1095–1098.

Manea, V.C., Manea, M., Kostoglodov, V., Sewell, G., 2005. Thermomechanical model of the mantle wedge in Central Mexican subduction zone and a blob tracing approach for the magma transport. Phys. Earth Planet. Interiors 149, 165–186.

Newton, R.C., Charlu, T.V., Kleppa, O.J., 1980. Thermochemistry of the high structural state plagioclases. Geochem. Cosmochim. Acta 44, 933–941.

Peacock, S.M., 1987. Serpentinization and infiltration metasomatism in the Trinity peridotite, Klamath province, northern California: implications for subduction zones. Contrib. Miner. Petrol. 95, 55–70.

Peacock, S.M., Wang, K., 1999. Seismic consequences of warm versus cool subduction metamorphism: examples from southwest and northeast Japan. Science 286 (5441), 937–939.

Pinkerton, H., Stevenson, R.J., 1992. Methods of determining the rheological properties of magmas at subliquidus temperatures. J. Volcanol. Geotherm. Res. 53, 47–66.

Plank, T., Langmuir, C.H., 1998. The chemical composition of subducting sediment and its consequences for the crust and mantle. Chem. Geol. 145, 325–394.

Poli, S., Schmidt, M.W., 2002. Petrology of subducted slabs. Annu. Rev. Earth Planet. Sci. 30, 207–235.

Powell, R., Holland, T., 1999. Relating formulations of the thermodynamics of mineral solid solutions: activity modeling of pyroxenes, amphiboles, and micas. Am. Miner. 84, 1–14.

Ramberg, H., 1981. Gravity, Deformation of the Earth's Crust in Theory, Experiments and Geological Applications. Academic Press, New York, 214 pp.

Ranalli, G., 1995. Rheology of the Earth. Chapman and Hall, London, 413 pp.

Regenauer-Lieb, K., Yuen, D.A., Branlund, J., 2001. The initiation of subduction: criticality by addition of water? Science 294, 578–580.

Rudolph, M.L., Gerya, T.V., Yuen, D.A., DeRosier, S., 2004. Visualization of multiscale dynamics of hydrous cold plumes at subduction zones. Visual Geosci. 17, doi:10.1007/s10069-004-0017-2.

Rupke, L.H., Morgan, J.P., Hort, M., Connolly, J.A.D., 2004. Serpentine and the subduction zone water cycle. Earth Planet. Sci. Lett. 223, 17–34.

Scambelluri, M., Philippot, P., 2001. Deep fluids in subduction zones. Lithos 55, 213–227.

Schmidt, M.W., Poli, S., 1998. Experimentally based water budgets for dehydrating slabs and consequences for arc magma generation. Earth Planet. Sci. Lett. 163, 361–379.

Scott, D.R., Stevenson, D.J., 1986. Magma ascent by porous flow. J. Geophys. Res. 91, 9283–9296.

Smith, G.P., Wiens, D.A., Fischer, K.M., Dorman, L.M., Webb, S.C., Hildebrand, J.A., 2001. A complex pattern of mantle flow in the Lau backarc. Science 292, 713–716.

Spiegelman, M., Kelemen, P.B., 2003. Extreme chemical variability as a consequence of channelized melt transport. Geochem. Geophy. Geosyst. 4, art. no. 1055.

Staudigel, H., Hart, S., Schmincke, H., Smith, B., 1989. Cretaceous ocean crust at DSDP sites 417-418: Carbon uptake from weathering versus loss by magmatic outgassing. Geochim. Cosmochim. Acta 53, 3091–3094.

Stern, R.J., 2002. Subduction zones. Rev. Geophys. 40, 3-1–3-38.

Tamura, Y., 1994. Genesis of island-arc magmas by mantle-derived bimodal magmatism—evidence from The Shirahama Group, Japan. J. Petrol. 35, 619–645.

Tamura, Y., Tatsumi, Y., Zhao, D.P., Kido, Y., Shukuno, H., 2002. Hot fingers in the mantle wedge: new insights into magma genesis in subduction zones. Earth Planet. Sci. Lett. 197, 105–116.

Thompson, A.B., Connolly, J.A.D., 1995. Melting of the continental-crust - Some thermal and petrological constraints on anatexis in continental collision zones and other tectonic settings. J. Geophys. Res. 100, 15565–15579.

Thompson, J.B., Hovis, G.L., 1979. Entropy of mixing in sanidine. Am. Miner. 64, 57–65.

Vasilyev, O.V., Podladchikov, Y.Y., Yuen, D.A., 1998. Modeling of compaction driven flow in poro-viscoelastic medium using adaptive wavelet collocation method. Geophys. Res. Lett. 25, 3239–3242.

Vasilyev, O.V., Gerya, T.V., Yuen, D.A., 2004. The application of multidimensional wavelets to unveiling multi-phase diagrams and in situ physical properties of rocks. Earth Planet. Sci. Lett. 223, 49–64.

Wei, C.J., Powell, R., 2003. Phase relations in high-pressure metapelites in the system KFMASH (K_2O-FeO-MgO-Al_2O_3-SiO_2-H_2O) with application to natural rocks. Contrib. Miner. Petrol. 145, 301–315.

White, R.W., Powell, R., Phillips, G.N., 2003. A mineral equilibria study of the hydrothermal alteration in mafic greenschist facies rocks at Kalgoorlie, Western Australia. J. Metamorphic Geol. 21, 455–468.

Zhao, D.P., 2001. Seismological structure of subduction zones and its implications for arc magmatism and dynamics. Phys. Earth Planet. Interiors 127, 197–214.

Zhao, D.P., Hasegawa, A., Horiuchi, S., 1992. Tomographic imaging of P and S wave velocity structure beneath north-eastern Japan. J. Geophys. Res. 97, 19909–19928.

Zhao, D.P., Mishra, O.P., Sanda, R., 2002. Influence of fluids and magma on earthquakes: seismological evidence. Phys. Earth Planet. Interiors 132, 249–267.